Shear profiles and localization in simulations of granular materials

Einat Aharonov
Weizmann Institute of Science, Rehovot 75100, Israel

David Sparks
Department of Geology and Geophysics, Texas A&M University, College Station, Texas 77843

(Received 19 June 2001; published 16 May 2002)

We present results from two-dimensional computer simulations of shearing granular layers, using a discrete element code, and applying a wide range of boundary conditions. We specifically investigate the distribution of shear within the granular layer and find two different modes of localization depending on the applied shear velocity, pressure, and layer thickness: (1) granular layers that develop a persistent shearing boundary region (''fluidlike'' behavior) and (2) layers that switch between diffuse deformation and randomly positioned internal shear bands (''solidlike'' behavior). The two end-member deformation modes can be found in laboratory experiments performed under low and high confining pressure, respectively. Micromechanical investigation reveals two different statistical distributions of the grain contacts correlating with the two different shearing modes. These results imply that rehological transitions in granular flow modes are linked to quantifiable microtstructural organization.

DOI: 10.1103/PhysRevE.65.051302 PACS number(s): 45.70.−n, 83.80.Fg

I. INTRODUCTION

Despite over a century of research in the mechanics of granular media (dating back to Reynolds in 1885 [1]), there is still no consistent, general physical or mathematical formalism that successfully predicts the collective behavior of a large number of discrete grains [2]. Even for simple two-dimensional shear of grains confined between parallel plates (see Fig. 1 for a picture of the system studied) there is no consistent description of motion of the granular layer. The problem is very basic (the analog in fluids is Couette flow) and has wide industrial applications. It is also of interest to earth scientists, since the fragmented rock layer (termed ''gouge'') within a geological fault, which is basically a shearing granular layer, is often the site of earthquake nucleation and rupture. Thus description of shear in granular layers is closely linked to understanding earthquake physics.

Experimental observations of shearing granular layers are varied. In general, two different end-member behaviors are reported depending mainly on the confining pressure (normal stress P applied to the bounding walls of the layer). Under low confining pressure a boundary layer of grains undergoing high shear forms near the moving wall, remaining spatially and temporally constant [3]. On the other hand, under high pressure, shear is initially distributed throughout the layer and then localizes in internal shear bands (e.g., [4]). This localization is thought to coincide with grain crushing. Grain-size reduction within the localized shear bands is thought to help lock the shear to a particular narrow region. However, under continued strain, shear is observed to switch again to its diffuse mode [5]. In experiments of shearing fault gouge [6] and in simulations [7] localization coincides with the onset of velocity-weakening behavior of friction, in which the shear stress supported by the layer decreases with increasing shear velocity, while diffuse deformation is usually associated with velocity strengthening. Thus it is clear that the issue of shear distribution within a granular layer is important for understanding macroscopic properties of the shearing aggregate, such as its strength in resistance to shear.

An important issue in determining a macroscopic description is the role of microscopic (grain-scale) fluctuations. It has recently been recognized that an important characteristic of granular packings is the heterogeneity in the forces between particles [8–11]. In a densely packed granular layer, stress will be transmitted across the system by a network of

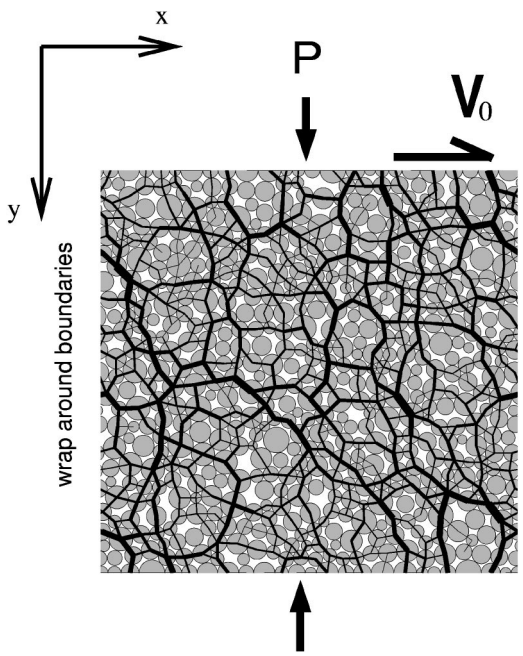

FIG. 1. A representative numerical simulation of a granular aggregate. This system contains approximately 24×24 grains, shown as gray circles. The direction and magnitude of contact forces between grains are shown by black lines. The simulation conditions are constant confining pressure P applied to the top and bottom boundaries, periodic horizontal boundaries, and constant velocity V_0 applied to the upper boundary.

''force chains,'' or sublinear sets of grains which interact through long-lasting contacts that each carry up to several times the mean contact force (see Fig. 1 for a visual representation of force chains). Force chains tend to preferentially align with the direction of maximum compressive stress in the system. In granular materials confined by forces applied on the boundaries, force chains always exist, since they are what maintains the volume of the layer against applied forces. During shear, individual chains are created and destroyed very rapidly, at a rate even larger than large-scale grain rearrangement [12]. In describing the strength of a granular material, much attention has been focused on observations and descriptions of force chains, e.g., [13–15]. However, the majority of grains in the layer will lie between force chains and may weakly interact with the force chains and with each other (''spectator'' grains) [16].

In this paper we present results from numerical simulations where we shear a layer of two-dimensional (2D) disks confined between two rough and rigid walls. We investigated modes of shear and shear localization under a variety of pressures applied to the boundary, system sizes, and driving velocities, and compare the results to experimental findings.[1] We find two distinct modes of deformation: shear reminiscent of fluidlike deformation and shear similar to solidlike deformation. We present a phenomenological description of the phase space for granular behavior under shear and evidence that the statistical characteristics of microscopic grain to grain contacts has bearing on the mean, large-scale, behavior of the granular medium.

II. MODEL DESCRIPTION

Grain aggregates are numerically modeled using a version of the discrete element method [17] which treats grains as inelastic disks with rotational and translational degrees of freedom. Gravity is not applied in the simulations reported here. The numerical model and conditions used are similar to our previous work [12]. The centers of two grains i and j are separated by a vector $\mathbf{r}_{ij}$. When the distance between centers r_{ij} is less than the sum of the two radii R_i and R_j, the grains undergo an inelastic interaction. During the interaction both grains experience a contact force that has shear F^s and normal F^n components. The normal component consists of a linear elastic repulsive force and a damping force dependent on the relative grain velocities $\dot{\mathbf{r}}_{ij}$:

$$F^n{}_{ij}(t)=[k_n(R_i+R_j-r_{ij})-\gamma_n m(\dot{\mathbf{r}}_{ij}\cdot\hat{\mathbf{n}})]\hat{\mathbf{n}}. \tag{1}$$

Here $\hat{\mathbf{n}}=(\mathbf{r}_{ij}\cdot\hat{\mathbf{x}},\mathbf{r}_{ij}\cdot\hat{\mathbf{y}})/r_{ij}$ is the unit vector parallel to the contact. k_n is the normal elastic constants, m is the grain mass, and γ_n is a damping coefficient ensuring inelasticity of the interaction. Shear forces on contacts are determined using an elastic/friction law [17]

$$F^s{}_{ij}(t)=-\{\min[k_s\Delta s,\mu(\mathbf{F}\cdot\hat{\mathbf{n}})]\}\hat{\mathbf{s}} \tag{2}$$

where $\hat{\mathbf{s}}=(\mathbf{r}_{ij}\cdot\hat{\mathbf{y}},-\mathbf{r}_{ij}\cdot\hat{\mathbf{x}})/r_{ij}$ is the unit vector tangent to the contact. μ is the surface friction coefficient, k_s is the shear elastic constant, and Δs is the shear displacement since the formation of the contact. Positions of the centers of mass of the disks are calculated using Newton's law and summing over all contacts J between grains:

$$m_i\frac{d^2\mathbf{x}_i}{dt^2}=\sum_{j=1}^{J}\mathbf{F}_{ij}. \tag{3}$$

In addition to motion of the center of mass of the disks we also calculate the rotation of each disk, in terms of its relative angular position ϕ_i, where I_i is the moment of inertia:

$$I_i\frac{d^2\phi_i}{dt^2}=\sum_{j=1}^{J}F^s_{ij}R_i. \tag{4}$$

Nondimensional distance is scaled to the average disk diameter $\hat{x}=2\overline{R}$. Time is scaled to the undissipated elastic wave travel time $\hat{t}=\sqrt{\hat{m}/k_n}$, where $\hat{m}$ is the mass of a disk of diameter $\hat{x}$. Velocity is scaled to the undissipated elastic wave speed $\hat{V}=\hat{x}/\hat{t}$. Stress is scaled to the elastic modulus of the system σ_0, so that a pressure $P=1$ is equivalent to $\approx 10^5$ MPa, when using a characteristic Young's modulus for rocks (e.g., quartz). We will use nondimensional parameters from now on.

III. SIMULATION CONDITIONS

In the simulations presented here $k_n=1$, $k_s=0.5$, $m=1$, and $\mu=0.5$. Systems are highly damped with $\gamma=1$ corresponding to a normal restitution coefficient of ~ 0.3 [12]. Simulations are performed on rectangular systems with $nt=nx\times ny$ disks. The top and bottom edges of the box are composed of grains glued together to form rigid rough walls of length nx (Fig. 1). The granular layer is periodic in the horizontal direction. Grain radii are randomly drawn from a Gaussian distribution that peaks at $\overline{R}$, with a standard deviation of $0.5\overline{R}$. Polydispersivity is introduced to discourage ordering effects. Systems are initiated as tall loosely packed boxes, which are compacted vertically by application of pressure to the boundary until reaching a height ny, ranging from 24 to 96 grains.

After compaction and relaxation of residual stresses (as explained in [12]) we apply a pressure P (ranging from 10^{-6} to 10^{-3}) to the upper and lower walls, and move the top wall in the x direction by applying a constant velocity V_0 at $y=0$, ranging between 10^{-3} and 10^{-4} of the wave speed. The systems then evolve to have a preferred unique (''critical'') porosity around which they fluctuate, dilating and compacting slightly during shear [12]. This porosity is not directly correlated with the pressure applied to the boundary, and

[1] In the simulations presented here porosity is not prescribed *a priori*. After application of constant pressure P and shear velocity V_0 to the boundary, systems evolve to a porosity state which is more or less constant, and which has a value characteristic of the marginal stability porosity [12].

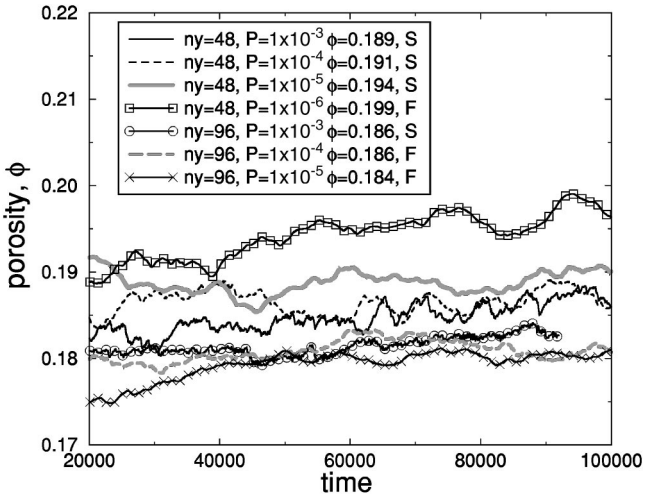

FIG. 2. Porosities from numerical experiments. Average values denoted by ϕ are given in the legend. Standard deviations of porosities range from 0.001 to 0.003 depending on the conditions of the run. Layer thickness and confining pressure are given in the legend by ny and P, respectively; here $nx=48$. Note that thicker layers have smaller porosities, and that in the thick layer, $ny=96$, there is no consistent trend of increasing porosity with decreasing confining pressure. The letters *F* and *S* in the legend indicate the observed mode of shear, as discussed in Sec. IV.

some runs with higher pressure have higher porosity than runs that are more weakly confined, as seen in Fig. 2. Porosity is insensitive to the applied confining pressure because shearing is performed here under ''rigid limit'' conditions (i.e., elastic deformation of grains is smaller than about 1%), which results in achievement of a ''marginal rigidity porosity,'' a porosity state that was identified previously as an attractive phase boundary associated with a macroscopic rigidity transition, where behavior of the aggregate transitions from fluidlike to solidlike as porosity is decreased beyond the critical value. Increasing pressure P in this state is accommodated not necessarily by porosity reduction but by changes in the granular contact network, as explained in [12], and as seen in the two different contact networks formed during shear under an order of magnitude change in pressure, Fig. 3.

IV. SIMULATION RESULTS

A. Velocity profiles

Applying different boundary conditions results in different shear profiles, and different overall behavior. The low end of the confining pressure regime ($P=10^{-6}$, which is equivalent to $P=60$ kPa for glass beads of size 1 mm) corresponds to the regime in which some laboratory experiments [18] are performed: stresses are low enough to generally not result in grain breakage, and indeed grains suffer little deformation. The highest confining pressure used ($P=10^{-3}$, equivalent to 60 MPa) is appropriate for geophysical simulations, corresponding to a burial depth of 2 km. Under the highest applied pressures, some of our numerical grains suffer a small ''elastic deformation'' approaching 0.5% of a grain diameter. In experiments of shear in rocks or glass beads, grain breakage often occurs at these stresses [19,20], an effect which is not included in the present model.

Figure 4(a) shows the instantaneous velocity vector (arrows) measured at some random time in the middle of two simulations using about 4600 grains. Horizontally averaged grain velocity $v(y)$ is plotted on top of the arrow plot, as a function of y, the depth from the shearing boundary (solid curves). The left plot is from a simulation with low confining pressure, $P=10^{-5}$, while the right had 100 times higher confining pressure, $P=10^{-3}$.

Figure 4(b) shows a few representative profiles of horizontally averaged velocity profiles $v(y)$ under the two different applied confining pressures, taken at different random times during the run. Note that the granular layer that is confined under lower P develops a shear layer adjacent to the

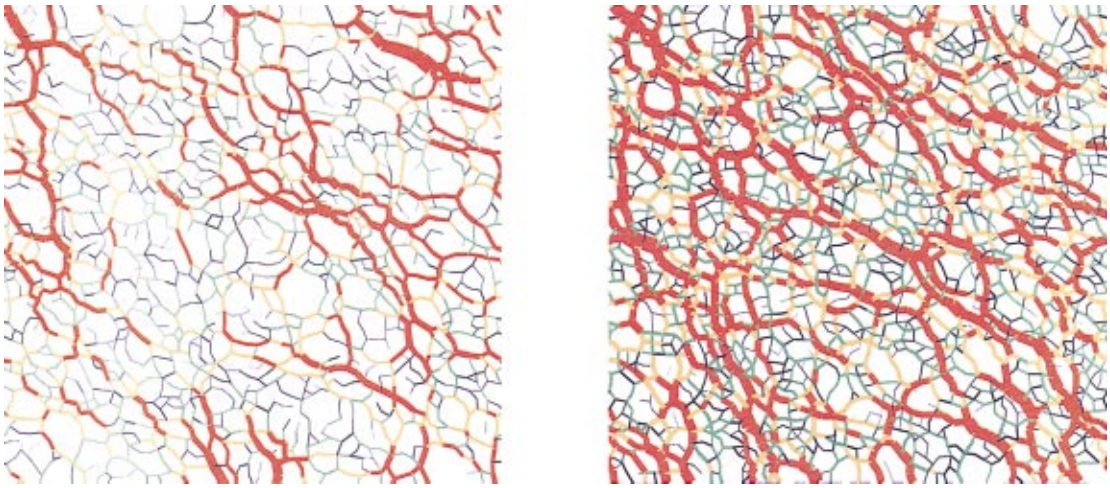

FIG. 3. (Color) Contacts between grains (grains are not shown), from a snapshot taken at a random time during two runs of a shearing layer with 48×48 grains ($V_0=10^{-3}$). The left is under pressure $P=10^{-4}$, while the right is from a simulation under $P=10^{-3}$. Line thickness is scaled to the highest stress in the frame. Contacts are color coded so that red, orange, green, and blue are contacts carrying scaled forces $f>1.5$, $1.5>f>1.0$, $1>f>0.5$, and $0.5>f$, respectively.

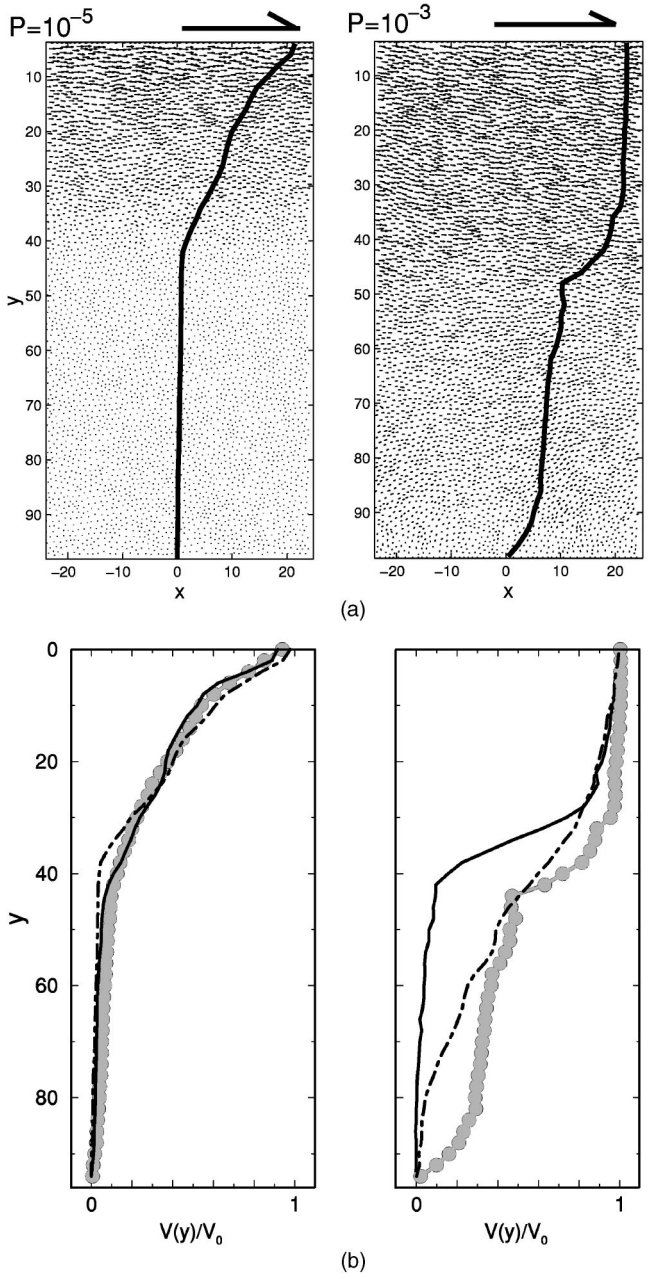

FIG. 4. (a) Individual grain velocity vectors (tiny arrows) and horizontally averaged velocities $v(y)$ (lines) as a function of depth away from the shearing wall from two simulations with a confining pressure of $P=10^{-3}$ (right) and $P=10^{-5}$ (left). Simulations use the same grain configuration (48 grains wide by 96 high), and the upper wall velocity is $V_0=10^{-3}$. (b) $v(y)$ at three different random times during the runs from the same two simulations in (a). Note persistent boundary shear (i.e., steep velocity gradient near the boundary) on the left, as opposed to migrating internal shear bands, alternating with diffuse shear, on the right.

moving wall, while the more highly confined granular layer on the right develops internal shear bands which migrate and alternate with diffuse (nearly uniform) shear. This is indeed a general trend: one of two different modes of shear distribution is observed in all the simulations we performed, depending on shear velocity, confining pressure, and layer thickness. The first shear mode, appearing under the lower confining pressure, faster velocity conditions which are usually used in physics experiments such as [18], is characterized by persistent localized deformation near the shearing wall (Fig. 4 left, $P=10^{-5}$). The second mode, appearing under geophysical experimental conditions, such as used by [21], is characterized by alternating periods of diffuse shear and transient shear bands localizing at random depths within the layer (Fig. 4 right, $P=10^{-3}$). The shear bands in this shear mode have a characteristic width of 10–20 grains. The location of an individual shear band may persist for times ranging between 250 and 25 000 time steps, which is equivalent to motion of the upper wall over a distance of 0.2–20 grain diameters. Once a shear band disappears a new one may appear at any subsequent time and at any depth. Systems shearing in this second mode characteristically spend about half the time in localized motion and the other half in distributed shear. The distribution, duration, and location of localization events are not trivial and merit future studies, which are beyond the scope of this paper.

We shall use the terms fluidlike and solidlike to distinguish the two modes of deformation since boundary layer deformation (including the linear profile induced by Couette flow, which is an extreme case of a boundary layer) is characteristic of fluids, while internal shear bands are generally associated with solids. We call the fluidlike mode of shear ''mode *F*'' and the solidlike mode of shear ''mode *S*.''

Figure 4 presents horizontal spatial averages. However, it contains much temporal variability, especially in the *S*-mode case where transient shear bands form and disappear. Therefore we performed long time averages (over 2×10^6 time steps, or an upper wall displacement of about 100 grains) of $v(y)$. $\overline{v}(y)$, where the overbar indicates temporal averaging (Fig. 5) shows clearly the two distinct modes of shear, where all of the simulations fall into one mode or the other.

(1) Fluidlike mode (mode F). This mode appears under lower confining pressure *P*, higher velocity V_0, and thicker layers (larger ny). Profiles of $\overline{v}(y)/V_0$ vs depth for all runs that exhibit this mode of shear are plotted in Fig. 5 (left). In these runs velocity decays away from the boundary in a near-exponential fashion. In fact, the numerical results agree with the theoretical prediction of [3], as shown by the lines on Fig. 5 (left):

$$\frac{\overline{v}(y)}{V_0} \propto \int_0^y \left(\cosh\frac{ny-y'}{\delta}\right)^{1/\alpha} dy', \tag{5}$$

where $\alpha=0.35\pm0.1$, in agreement with the experimental results presented in [3]. Two different fits are shown using length scales $\delta=36$ (black line) and $\delta=26$ (blue line), since the former fits better the layer 96 grains thick, while the latter fits better the layer 48 grains thick. In the Appendix we briefly outline the steps in the derivation of Eq. (5). For the thinnest layers, $ny=24$, the velocity profile decays faster than the theoretical prediction because the system size is smaller than the characteristic length scale δ.

(2) Solidlike mode (mode S). Under higher confining pressure *P*, slower velocities V_0, or when using smaller ny,

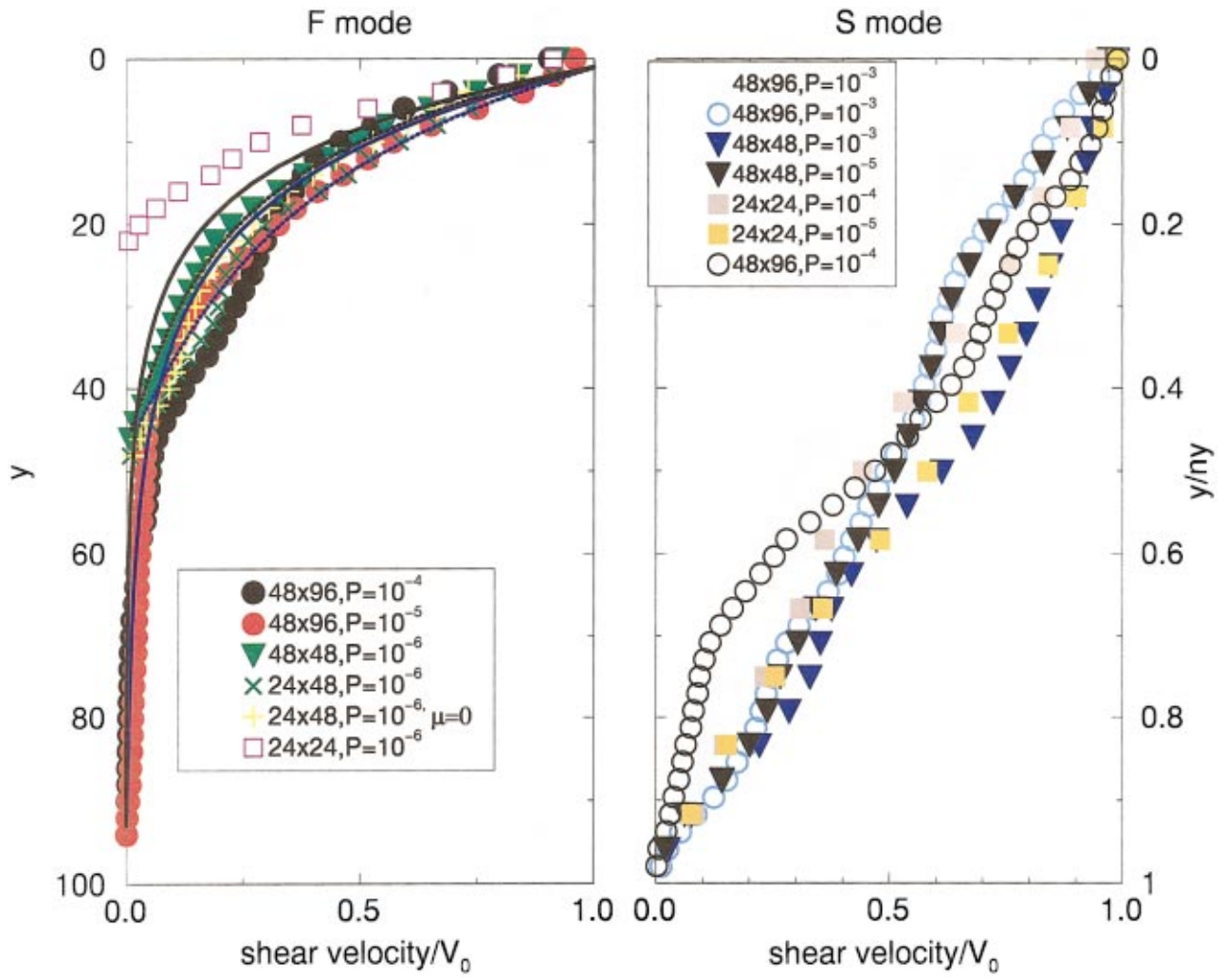

FIG. 5. (Color) Time-averaged horizontal grain velocities $\overline{v}(y)$ versus depth y. Open symbols are from runs with $V_0=10^{-4}$ and closed symbols from runs with $V_0=10^{-3}$. Pluses represent a run with $\mu=0$. Time-averaged velocity profiles are linear in mode-S deformation, while exponentially decaying in mode F. Theoretical fits for mode-F runs are given by Eq. (5), where blue lines use $\delta=26$ and black lines $\delta=36$, with dotted lines for a fit for a layer of $ny=48$ and solid for $ny=96$.

the boundary layer localization [Eq. (5)] of mode F disappears. Figure 5 (right) shows $\overline{v}(y)$ from all simulations that do not belong to mode F. In this second mode $\overline{v}(y)$ approaches a linear function, indicating that on average a uniform shear rate operates across the layer. This serves as a partial proof that the internal shear bands that are observed in this mode at different times and different places in the layer indeed migrate randomly, alternating with diffuse deformation.

To explore the effect of varying the different parameters of our model we also ran a set of simulations (with $ny=48$, $nx=24$, varying P between 10^{-3} and 10^{-6}) using zero friction between the grains ($\mu=0$). The frictionless layer had lower average porosity and shear stress compared to the layer with $\mu=0.5$. However, the temporally averaged velocity profiles were similar between $\mu=0.5$ and 0. An example of a frictionless run is given in pluses in Fig. 5 (left). Another parameter that we varied was γ, the normal damping coefficient, which controls the restitution coefficient. Simulations with reduced γ suggest that γ plays an insignificant role in determining the shear profile when $\mu>0$, probably because friction acts as a more significant energy sink than collisions in this tight packing limit. However, when $\mu=0$, γ has a significant effect on the shear profiles, which we did not explore.

B. Phase diagram

The layer thickness ny is important in determining where the transition between mode S and mode F occurs—the thicker the layer the easier it is to ''fluidize,'' and so it remains in mode F under higher confining pressures, as seen in Fig. 5. Figure 6 schematically shows the phase diagram in layer thickness versus confining pressure. The effect of horizontal layer extent nx was also explored by running simulations of sizes 48×24, and 24×48 and comparing to simulations with layers of 24×24 and 48×48. As far as we can determine, the horizontal extent of the layer (which has wraparound boundary conditions) did not affect the outcome.

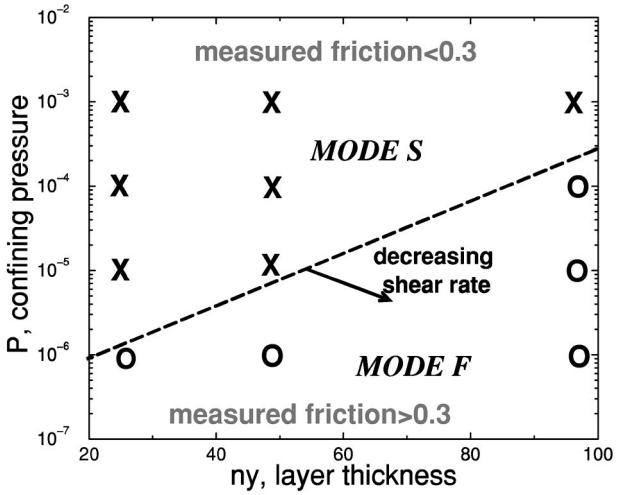

FIG. 6. Schematic phase space for the two different behaviors of the system: mode *F* (circles) and mode *S* (crosses). As the layer gets thicker it is easier to fluidize even under higher confining pressures. Apparent friction changes slightly across the phase boundary.

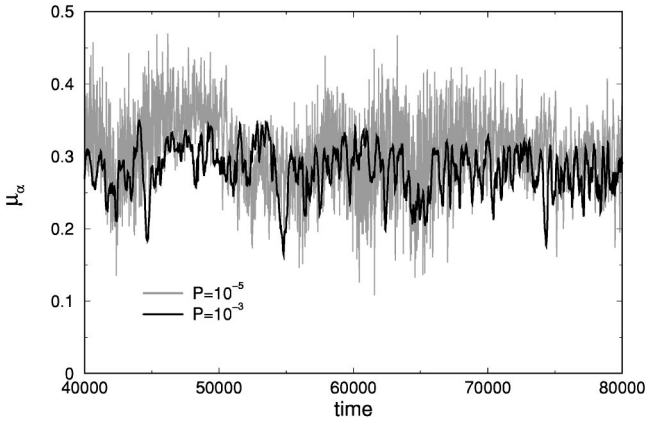

FIG. 7. Representative apparent friction μ_a (measured shear stress normalized by the applied confining pressure) from two numerical simulations of 48×96 granular aggregate sheared at $V_0=10^{-3}$, but using two different confining pressures $P=10^{-3}$ and $P=10^{-5}$. Observe that the apparent friction has very similar values despite the two orders of magnitude difference in applied confining pressure.

Granular systems with size 48×48 behaved identically to those of 24×48, i.e., to layers with half the horizontal extent, e.g., they both showed the *F* mode when $P=10^{-6}$, and the *S* mode for higher confining pressures. Also, a layer that was twice as long as it was thick (48×24), was similar to a square one (24×24).

In the experiments shown in Fig. 6, $V_0=10^{-3}$. We did not extensively explore the effect of shear velocity on the phase boundary (because of the long time it takes to simulate slow shear), but we observe that increasing V_0 causes the phase boundary to migrate toward higher normal stresses and thinner layers. In particular, for the marginal case of a 48×96 layer under $P=10^{-4}$ when $V_0=10^{-3}$, the system is in mode *F* as shown by filled black circles in Fig. 5, but when using a ten times slower shear velocity of $V_0=10^{-4}$ the velocity profiles are mode *S*, as shown by open black circles in Fig. 5.

Several measures were investigated to search for the source of this mode switching: first the average and depth dependent measures of the systems, porosity, coordination number (average number of contacts per grain), and stress power spectra. However, not much difference appears between macroscopic measures of systems shearing in the two modes. For example, the variation of time-averaged porosity among all the simulations is about 1%, and the variation is not systematic (see Fig. 2). Porosity in low confining pressure runs may be either higher or lower than porosity in high confining pressure runs.[2] A second measure, the average coordination number in the layer, does decrease with decreasing *P*, but does not correlate with the shear mode.

[2]However, there is a tendency for thinner layers to have higher porosity than thicker layers (e.g., on average, 0.191 pore fraction in 48 thick layers, 0.185 in 96 thick layers). This is expected since the shear-induced dilation should be related to the ratio of grain size to system size.

We also examined the time series of the shear stress measured on the moving wall, normalized by the applied confining pressure *P* (Fig. 7). This ratio of stresses describes the apparent friction coefficient of the layer μ_a. Friction has some correlation with the mode of deformation, where generally higher values (with a time average slightly larger than 0.3) are seen for mode-*F* runs than for mode-*S* runs (time average ranging between 0.28 and 0.3). Also, fluctuations in stress change with changing boundary conditions: the friction time series appear spiky at low *P* and varies more slowly with time at higher *P* [12].

The final macroscopic measure investigated is the power spectrum Σ of the stress time series measured at the walls. An example of such a time series is given by Fig. 7. Simulation results show that Σ is a power law function of frequency ω, $\Sigma(\omega)\propto\omega^{\eta}$. The exponent η is found to be only a function of the confining pressure *P*, and not of the shear mode. Plots of $\Sigma(\omega)$ vs ω for a variety of confining pressures are shown in [12]. This insensitivity of the stress power spectrum to the mode of deformation is in line with the insensitivity of all other macroscopic measures we tried.

C. Micromechanics

We next investigate the grain to grain contact distribution, to understand the micromechanical source for the two distinct modes of shear. Representative snapshots of contacts and stresses on contacts in an *F*-mode and in an *S*-mode run are given in the left and right frames of Fig. 3, respectively. We investigate the distribution of forces transmitted by such individual granular contacts, distributions of the contact directions, and sliding on these contacts. Results are presented from two representative runs using a layer of size of 48×96: a mode-*S* run sheared under $P=10^{-3}$ and a mode-*F* run sheared under $P=10^{-5}$.

Force distributions can be viewed by a histogram of normalized forces $f=F/\langle F\rangle$ on the contacts (Fig. 8), where $\langle F\rangle$

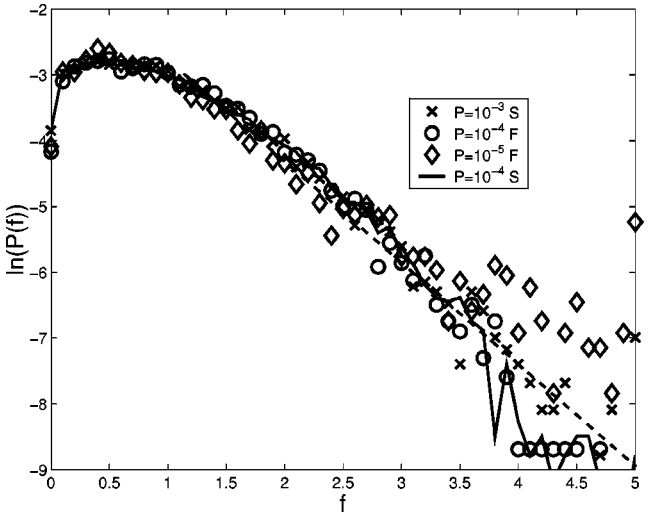

FIG. 8. Force histograms for three shear runs using three different applied stresses (in symbols) sheared at $V_0=10^{-3}$, and one run (solid line) sheared at $V_0=10^{-4}$. The mode of shear is indicated by *F* and *S* in the legend. Simulation results show invariance of the force distribution under varying boundary conditions and shear modes. The dashed line is a fit of Eq. (6), with $\beta=1.47$.

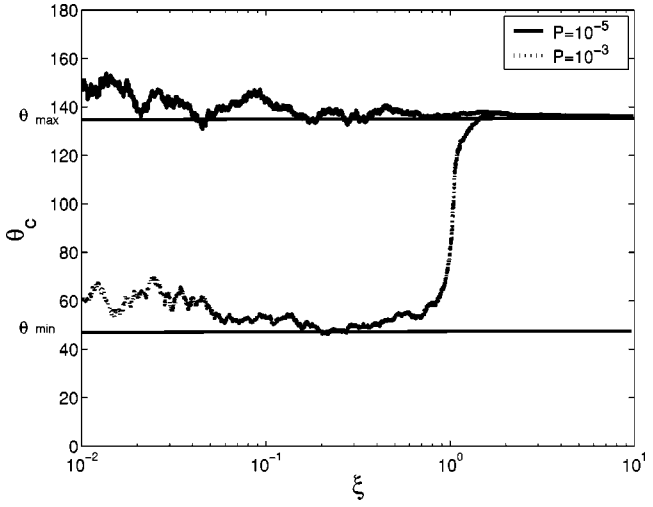

FIG. 9. Principal contact directions θ_c in the ξ network as a function of ξ for an *F*-mode run (using $P=10^{-5}$) and for a run exhibiting *S*-mode shear (using $P=10^{-3}$). Note the bimodal distribution of contact directions (transition around $\xi\approx 1$) for $P=10^{-3}$, the *S*-mode run, as opposed to nearly uniform contact directions for $P=10^{-5}$, the *F*-mode run.

is the spatially averaged force carried by contacts in the system. Figure 8 shows that the distribution of forces is invariant under different applied confining pressures and varying shear velocity. In each run the magnitudes of forces transmitted by grain contacts vary by at least two orders of magnitude. An exponentially decaying probability exists for finding forces greater than the mean force $f>1$, where

$$P(f)\propto \exp(-\beta f) \tag{6}$$

with $\beta=1.47\pm 0.1$. The observed force distribution agrees with simulations [22] and experiments [23] for quasistatic and static granular media. The invariance of force distributions under different loads and velocities is interesting and merits further studies. The partitioning of forces between contacts appears to be a basic property of the granular aggregate, independent of the boundary condition. Force distributions remain robust even under varying modes of shear and orders of magnitude change of mean stresses.

Figure 8 demonstrates that a diminishing number of large forces leads to poor statistics in the large-force intervals. Thus we follow the method suggested by Radjai *et al.* [24] and look at a subset of contacts carrying a force smaller than a cutoff value ($f<\xi$), and call this subset the "ξ network." This method of analyzing the contact force statistics is applied successfully to investigate the source of the difference between the *F* and *S* modes of shear.

The contact network that forms is characterized by the probability density function $E(\theta,\xi)$ of finding a contact with direction θ in the ξ network. We define the contact angle $\theta=\arctan[(\mathbf{r}_{ij})_x/(\mathbf{r}_{ij})_y]$, where $(\mathbf{r}_{ij})_a$ is the component in the *a* direction of the vector connecting the centers of grain *i* and *j*. Because the directions θ and $\theta+\pi$ are physically equivalent $E(\theta)$ may always be represented by a Fourier series containing even components. Dropping higher order terms, $E(\theta)$ can be written as [25]

$$E(\theta,\xi)=\frac{1}{2\pi}\{1+A_c(\xi)\cos[\theta-\theta_c(\xi)]\}. \tag{7}$$

The coefficient A_c is the amplitude of anisotropy, while θ_c is the principal direction. We calculate from the numerically obtained contact network the fabric tensor $\phi_{ab}(\xi)=\langle n_a n_b\rangle_\xi$, where n_a is the *a* component of the unit vector along the contact direction. Averaging for $\langle n_a n_b\rangle_\xi$ is over all contacts in the ξ network. We then use relationships such as

$$\langle n_x n_y\rangle=\int_0^{2\pi} E(\Theta,\xi)\cos\Theta\sin\Theta\, d\Theta$$

$$=\frac{A_C}{4}\sin 2\theta_c \tag{8}$$

to calculate $A_c(\xi)$ and $\theta_c(\xi)$ (see [24] for more details).

1. Contact directions and anisotropy

Similar to the results of [24] we find that a natural transition occurs at a cutoff value of $\xi=\xi_0$, which in some cases is approximately the average force, so that we define "weak" networks with $\xi<\xi_0$ and "strong" networks which have $\xi>\xi_0$.

In both *S* and *F* modes the direction of anisotropy of the entire set of grain to grain contacts ($\xi\to\infty$) is about 135° from horizontal (Fig. 9), in the expected direction θ_{max} of the maximum compressive stress σ_1 (see Fig. 10 for a schematic view of the principal directions). This direction θ_{max} is due to orientation of the "strong" contacts, those in force chains, which belong to networks of $\xi>\xi_0$. Surprisingly, the difference between the *S* and *F* modes is in the weak contacts

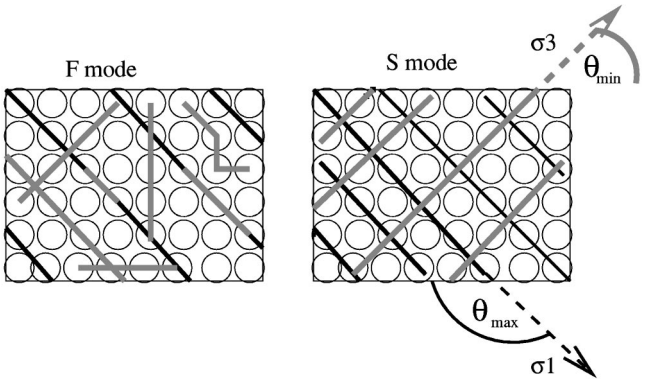

FIG. 10. Schematic view of the difference in network organization in granular media between the *F* mode of deformation (left) and the *S* mode (right). Both modes of shear have contacts which carry large forces (''stress chains'' drawn in black lines) oriented in the maximum compressive direction σ_1. However, the *S* mode is characterized by a supporting weak contact network (drawn in gray lines) which is roughly perpendicular to the stress chains, in the direction of σ_3. This network provides rigidity and supports the system against buckling. In contrast, the *F* shear mode lacks such a supportive weak network.

which dominate networks with $\xi<\xi_0$. In the *S* mode there exists a bimodal distribution of contact orientations: the weak networks have an orientation nearly perpendicular to θ_{max}, in the direction of minimum compression θ_{min}. The weak contact population is very important in that it contributes to the rigidity of the system and prevents buckling of the chains, as schematically shown in Fig. 10.

However, in systems shearing in mode *F*, the weak contacts do not provide rigidity, since they are not preferentially oriented normal to the strong contacts and therefore there is no ''mesh'' which provides bracing for force chains. Instead, some of the weak contacts participate in stress chains, while the rest of the weak contacts are nearly randomly oriented. Thus there is no clear distinction between strong stress chains and a weak supportive population as in mode *S*. Figure 10 is a schematic drawing to illustrate this point while Fig. 3 shows true snapshots of contacts from *S* (right) and *F* (left) runs.[3] Notice in Fig. 3 that in the *F*-mode frame many green and blue (i.e., ''weak'') contacts participate in stress chains, while in the *S*-mode frame the stress-chain direction ($\approx\theta_{max}$) is dominated by red (''strong'') contacts.

In viewing the direction of contacts the degree of anisotropy A_c must also be considered (Fig. 11). A_c increases roughly in proportion to the difference between the number of contacts oriented parallel to θ_c and perpendicular to it. In both shear modes the degree of anisotropy is large for the weak contacts and for the entire contact network. There is a

[3]All mode-*F* runs had a weak population with a preferred orientation in the direction of θ_{max}. However, not all *S*-mode runs have a weak population oriented in the θ_{min} direction. In some runs shearing in the *S* mode (those with conditions close to the transition to *F*-mode shearing) the weak population has an intermediate orientation, between θ_{min} and θ_{max}.

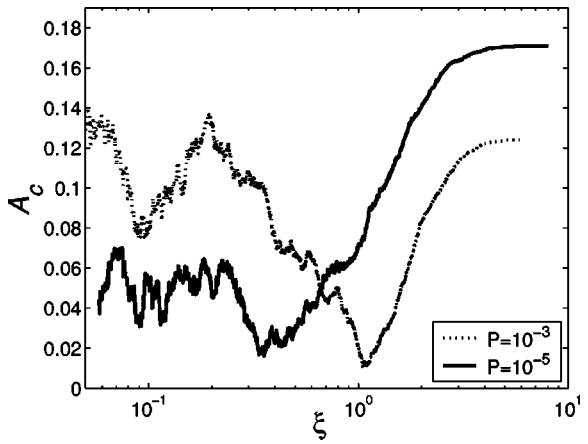

FIG. 11. Amplitude of anisotropy A_c in the ξ network as a function of ξ for an *F*-mode run ($P=10^{-5}$) and an *S*-mode run ($P=10^{-3}$).

minimum in anisotropy for the $\xi_0\sim1$ network for the *S*-mode case and $\xi_0\sim0.2$ network for the *F*-mode case. For the *S* mode, this minimum in anisotropy comes about because there is a bimodal distribution, with weak contacts preferentially oriented along θ_{min} and strong contacts along θ_{max}. At the minimum value for A_c, just enough large forces are included in this network that the two orientations nearly cancel.

2. Sliding and rolling

In both shear modes a larger proportion of the weak contacts undergo frictional sliding relative to the strong contacts. In fact, contacts with $f>1$ rarely, if ever, slide (Fig. 12). This is not surprising, since contacts with smaller *f* will reach the Coulomb sliding condition at lower shear forces. This is in agreement with simple shear simulations [24] where slip and dissipation occur mainly in the weak population. Overall, frictional sliding is more prevalent in *F*-mode shear than in *S*-mode shear (Fig. 12), despite the fact that *S*-mode shear

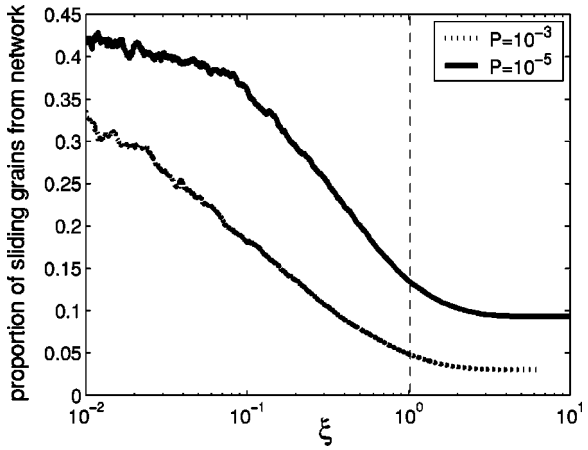

FIG. 12. Fraction of sliding grains in the ξ network as a function of ξ for two different normal loads, showing increased sliding for decreasing *P*. Note that in both cases mostly the ''weak'' contacts (those belonging to $\xi<1$ networks) slide.

characterizes deformation under more confined conditions. This trend also explains the slightly larger values of apparent friction measured in *F*-mode shear.

When sliding is hampered, either by confining pressure or reduction of possible rearrangements in a thin layer, grain rolling becomes a way of accommodating strain [7,26,27]. The location of the maximum rolling is near the position of highest shear, as expected: near the moving boundary for the *F* mode of shear and in the shear bands for the *S* mode [see Fig. 13(a)]. However, in terms of overall grain rolling, the two modes are different only in those grains that lie at the outskirts of the angular velocity distribution: There are more rapidly rolling grains (with $\omega/V_0 > 0.5$) in the *S*-mode runs than in the *F*-mode runs [Fig. 13(b)]. This rapid rolling stems from grain interlocking, and may compensate for lack of sliding by accommodating strain. Figure 13(a), which is a snapshot in time, demonstrates that all the rapidly rolling grains are confined within the shear zone. Thus we believe that, although the fraction of rapidly rolling grains is small, they might still play an important role in the deformation process, as was already observed in [26,28].

V. CONCLUSIONS

In this paper we have presented results from 2D simulations of shear in granular layers. We found two distinct modes of deformation where the transition is controlled by confining pressure, shear velocity, and layer thickness. The two modes are observed experimentally, but not much attention has been paid to the transition between them, and to the regimes that characterize each of them.

The first mode, which we termed fluidlike, or *F* mode for short, is characterized by persistent boundary layer shear, which is well predicted by a theoretical function. This mode is favored by applying lower confining pressures, higher shear velocity, and using thicker granular layers.

The second shear mode, characterized by solidlike (*S*-mode) behavior, is accompanied by localized shear bands that may appear at any depth including at the boundary. The system also spends about half of its time in nonlocalized, distributed, shear. This mode occurs under more confined conditions, slower shear, and thinner layers.

Our simulated systems operate in the rigid limit of granular packings, which is to say they experience only slight elastic deformation (under 1%). In this limit, shearing granular systems spontaneously evolve to have a preferred porosity which is very close to the marginal rigidity limit, the critical porosity that marks the boundary between solidlike and fluidlike behaviors [12]. For this reason all of our simulated systems have very similar porosity, not well correlated with the shear mode and confining pressure *P*. Increasing pressure on the boundary is accommodated by changes in the grain-contact network. The structure of the network of grain contacts also explains well and corresponds with the shear mode: In both *S* and *F* modes stress chains support the load in the maximum compressive direction. The transformation from *S*-mode shear to *F*-mode deformation is accompanied by decreasing lateral connections between stress chains. These lateral connections are made by the network of contacts carrying weak forces, which is preferentially aligned normal to the direction of the stress chains. In other words, when systems of grains behave as a solid, they have a ''weak force'' network oriented in the minimum compressive stress direction, and a complementary ''strong force'' network exists in the maximum compressive stress direction. In *F* mode the stress chains still exist, but the bimodal distribution and the supporting weak network disappears.

This mode switching in shearing is closely tied to the rigidity transition [12,29]. In [12] some simulations were conducted with the layer thickness fixed, not allowing dilation and compaction, so the porosity was constant. It was seen then that increasing the packing density of grains ν above a critical value ν_c causes a transition in both behavior of static packings and shearing systems: When $\nu < \nu_c$ systems shear in a ''gaslike'' manner, where no system-spanning stress chains occur, and grains interact by collisions [30]. Shear was localized in a boundary layer near the moving wall, similar to what we see in the *F* mode. When $\nu > \nu_c$, solidlike deformation occurred: system-spanning stress chains and localized shear in shear bands were observed. At $\nu = \nu_c$ the system flips between the two modes, jamming and unjamming intermittently, as described in [15]. In [12] we also found that ν_c is an attractive phase boundary when porosity is allowed to evolve freely under constant *P* boundary conditions.

But when the walls are free to compact and pressure is applied (even if it is infinitesimal) to the boundary, stress chains always form to support the applied load. In this case there cannot be a collision dominated gaslike regime, which can only emerge in the absence of connected chains. Despite the lack of this collision dominated gaslike phase, two modes of shear, which are fluidlike and solidlike in nature, still exist. But the lack of shear rigidity characterizing the *F* mode comes about not from lack of stress chains but from lack of a coherent structure supporting the stress chains.

The marginal porosity marks a phase boundary between loosely packed gaslike behavior, and compact solidlike behavior. Despite the fact that our simulated systems exist on this phase boundary on the porosity axis, we still find two distinct modes of rigidity. Transitions between these modes are activated by changing pressure, system size, and shear velocity, and can perhaps be viewed as crossing the phase boundary along these other axes rather than the porosity axis.

The transition between *F* and *S* modes under constant stress is linked to the ability of the system to dilate, and to the amount of sliding that occurs: The increment of work done on the system by applied deformation is defined as

$$dW = F^s d\gamma + P dh,$$

where the forces are measured on the moving wall, $d\gamma$ is the horizontal displacement of the wall, and dh is the change in layer thickness. When the confining pressure *P* is increased the work required to dilate the grain layer by dh increases. As Reynolds noted in his work on dilatancy, and as has been recently shown in experiments [18] and simulations [31], dilation is needed in order for sliding to occur. If *P* is decreased or layer thickness is increased (and therefore degrees

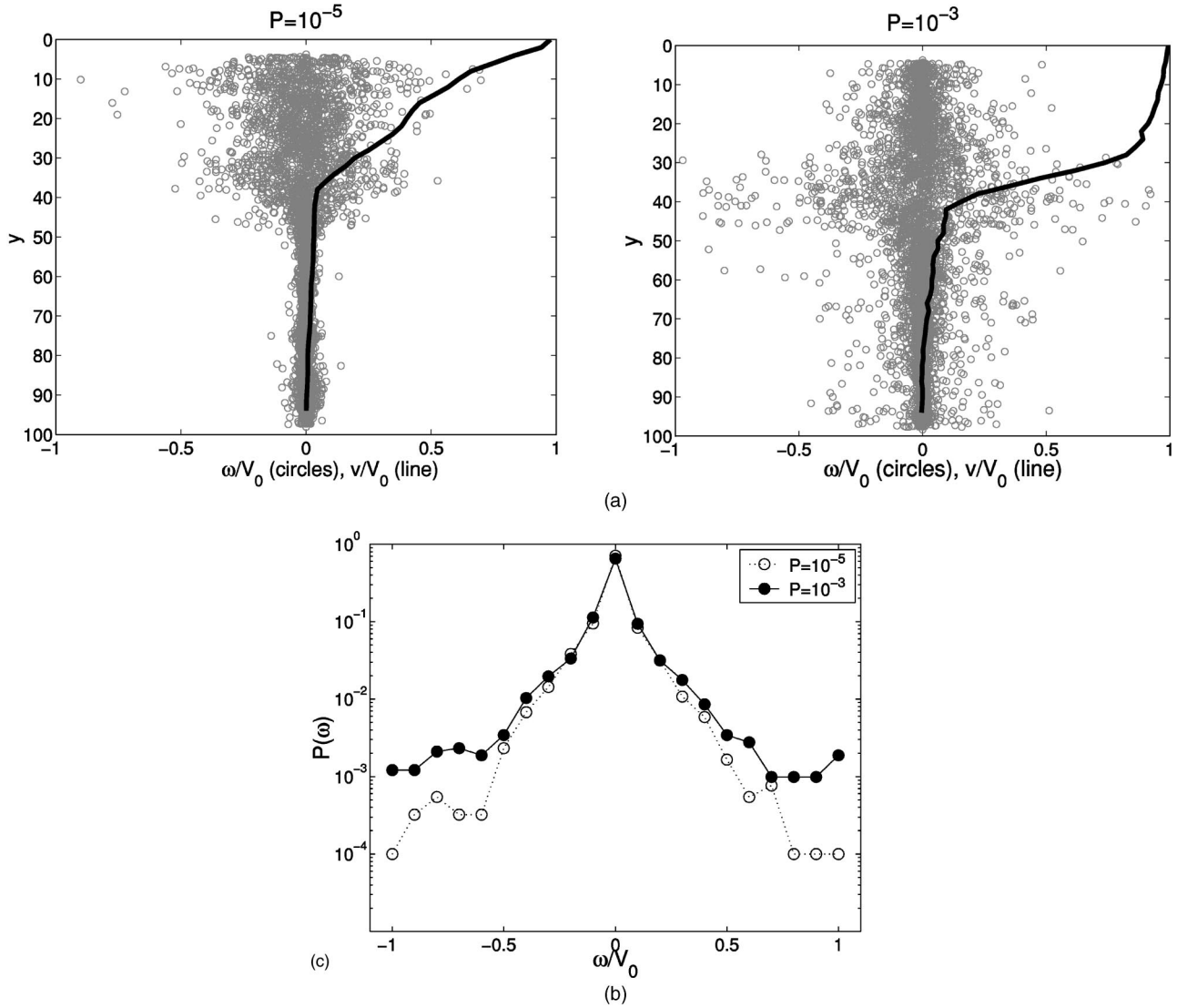

FIG. 13. (a) Instantaneous scaled angular velocities ω/V_0 of all grains in a 48×96 system in two shearing runs with $V_0=10^{-3}$. The angular velocity of each grain is plotted (circle) as a function of this grain's depth from the shearing boundary. On the left, results from an F-mode run ($P=10^{-5}$) and on the right an S-mode run ($P=10^{-3}$). Lines are horizontally averaged shear velocity profiles $v(y)/V_0$ at that time, showing that grain rotation is correlated with shear rate. (b) Histograms of angular velocity in the two runs, showing that the probability density function $P(\omega)$ of angular velocities for $|\omega/V_0|<0.5$ is similar in both modes. However, there are more grains with high rotational velocity $|\omega/V_0|>0.5$ in the S-mode run ($P=10^{-3}$) than in the F-mode run ($P=10^{-5}$). Rotation is an additional mode for accommodating strain.

of freedom and possibility of grain rearrangement increased), grain sliding within the layer becomes possible. Increasing shear velocity also produces grain sliding in our model because of the tangential force law we use, Eq. (2), where sliding is favored when the relative displacement between grains ΔS increases. This is also expected to be the case in real grain to grain contacts, since Eq. (2) mimics the transition from elastic deformation to sliding that is observed experimentally on contacts [32]. As reported, more sliding occurs in F mode and slightly more vigorous rolling in S mode. This naturally leads to a question of the role of grain geometry in this transition, since circular grains, as simulated here, will roll readily.

The results reported here are not expected to change qualitatively in 3D, as the experimental evidence [3,33] for the two distinct modes of deformation was obtained from 3D experiments. The position of the phase boundary is, however, expected to differ in 3D from 2D, since the rigidity transition occurs at a different porosity in 3D. Grain rolling is still expected to play a role in three dimensions, as is indirectly inferred in geological evidence of rounded grains found in granular shear zones such as in landslides, and as is directly observed in experiments in sand, e.g., [28].

It remains an open question to continue and investigate the mode of deformation and the related dissipation. The understanding of shearing modes of granular media presented in this paper is basic but is also important to earthquakes, where grains made up of crushed rocks are confined between rock walls and sheared during tectonic plate motion. It is possible that during an earthquake, which involves ac-

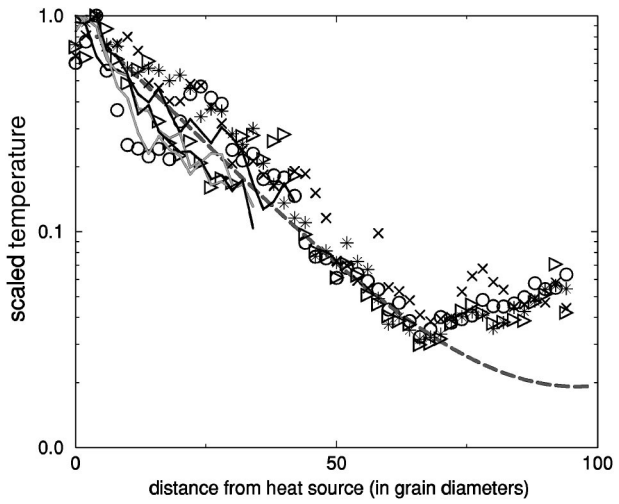

FIG. 14. Scaled temperature profiles as a function of distance from the heat source. Symbols are results from the *F*-mode run where distance is measured from the shearing wall ($y=0$). Solid lines show the temperature from the *S*-mode run, where a distance of 0 is taken as the instantaneous peak in shear rate, i.e., the shear band ''center.'' The dashed line is the theoretical prediction given by Eq. (A2), using $ny=96$ and $\delta=36$. The deviation of simulations from theory near the stationary wall (distance of 96) arises because shear at this boundary is an additional, unaccounted for, source of heat.

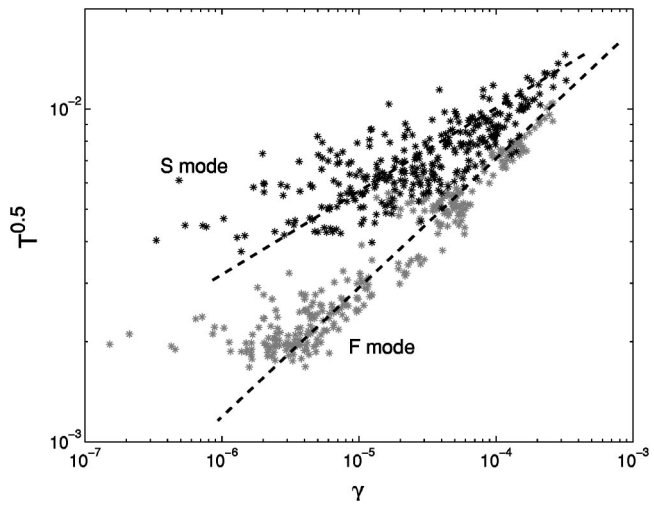

FIG. 15. Relation between $T^{0.5}$ and the shear rate γ; dark symbols are results from *S*-mode runs, light colored symbols from *F*-mode runs. Dashed lines show power-law relationships according to Eq. (A3) with $\alpha=0.2$ and 0.35, respectively.

celerating shear, the granular gouge changes its shearing mode from solidlike, *S* mode, to fluidlike, *F* mode, with increasing associated sliding and dissipation, which will affect sliding stability. In that case the understanding of changes in friction and dissipation will have implications in understanding earthquake rupture length.

Rheological transitions are also important in the study of stick-slip motion and sliding stability in granular materials [18]: In a recent study of granular layers undergoing stick-slip motion [34] we found that the locked period (''stick'') is associated with a buildup of a supportive weak network (as observed here for the *S* mode), while the ''slip'' phase is accommodated by the destruction of the weak network similar to the statistics of the *F* mode. It seems that an analytical framework which sets out to describe spatial and temporal behavior of granular materials should take into account these network structures that control the global behavior (a recent attempt is provided by [35]). In this context it is important to note that dilute systems, which lack a stress-chain network, are rarely found in naturally occurring granular systems. The majority of granular systems observed on Earth will maintain a connected set of contacts between grains since they operate under gravity or confining pressures. Examples include fault gouge, landslides, soils, coal in silos, and powders in chutes. Description of the deformation of connected networks is thus essential in natural granular systems.

ACKNOWLEDGMENTS

This work was funded by NSF Grant No. EAR-9804855. We wish to thank C. Scholz for helpful discussions.

APPENDIX: THEORETICAL DERIVATION OF VELOCITY PROFILES

In this appendix we outline the steps in calculating the predicted velocity profile given in Eq. (5), which was used to fit the *F*-mode velocity profiles. Solutions to Eq. (5), using $\alpha=0.35$, $\delta=26,36$, and $ny=48,96$ are drawn in lines in Fig. 5 (left). The following derivation is taken from [3].

The first step in the calculation of the mean velocity profile predicted for flow of granular materials is calculation of the profile of rms velocity fluctuations, the ''granular temperature'' *T*. Under steady-state shear temperature is assumed to obey a local heat conduction equation

$$\partial_y \lambda \partial_y T = \epsilon T, \tag{A1}$$

where λ and ϵ are the thermal conduction and energy loss rate, respectively. The solution to Eq. (A1), using constant heat supply at the boundary, $T=T_0$ at $y=0$, is

$$\left(\frac{T}{T_0}\right)^{1/2} = \frac{\cosh[(ny-y)/\delta]}{\cosh(ny/\delta)}, \tag{A2}$$

where $\delta^2=2\lambda/\epsilon$. Equation (A2) fits the temperatures profiles obtained in our simulations, as shown in Fig. 14. Figure 14 demonstrates that temperature profiles of both mode *S* and mode *F* are fitted by Eq. (A2), although in mode *S* the heat source T_0 must be taken as the internal shear band, since that becomes the location of maximum shear and heat.

Losert *et al.* [3] found experimentally, and we also find in our simulations, that an empirical power-law relation holds between the velocity fluctuations and the shear rate:

$$T^{1/2} \propto \left(\frac{\partial \overline{v}(y)}{\partial y}\right)^{\alpha}, \tag{A3}$$

where we find for *F*-mode runs $\alpha=0.35\pm0.1$ in close agreement with [3], but in contrast to the classic hydrodynami-

cally based argument leading to $\alpha=1$ (e.g., [30]). For a discussion of the deviation of α from 1, see [3]. We emphasize that *S*-mode runs also exhibit a power-law relationship, but with a different power from the *F* mode. Figure 15 shows the relation between temperature and shear from two simulations, one exhibiting *S*-mode shear, where $\alpha\approx 0.2$, and the other exhibiting *F*-mode shear, where $\alpha\approx 0.35$.

The last step in obtaining $\overline{v}(y)$ in Eq. (5) is the integration of Eq. (A3) with respect to *y*, using Eq. (A2). Fits are made only for *F*-mode simulations because in the *S* mode the source of heat migrates continuously throughout the layer. However, instantaneous velocity profiles of the *S* mode may be similarly reproduced using integration of Eq. (A3) and a value of $\alpha\approx 0.2$.

[1] O. Reynolds, Philos. Mag. **20**, 469 (1885).
[2] M. Jaeger, S.R. Nagel, and R.P. Behringer, Phys. Today **49**(4), 32 (1996).
[3] W. Losert, L. Bocquet, T. Lubensky, and J. Gollub, Phys. Rev. Lett. **85**, 1428 (2000).
[4] C. Marone and B. Kilgore, Nature (London) **362**, 618 (1993).
[5] N. Beeler, T. Tullis, M. L. Blanpied, and J. Weeks, J. Geophys. Res. B **101**, 8697 (1996).
[6] V. Scruggs and T.E. Tullis, Tectonophysics **295**, 15 (1998).
[7] P. Mora and D. Place, Geophys. Res. Lett. **26**, 123 (1999).
[8] B. Miller, C. O'Hern, and R. Behringer, Phys. Rev. Lett. **77**, 3110 (1996).
[9] C. T. Veje, D. W. Howell, R. P. Behringer, S. Scholmann, S. Luding, and H. Herrmann, in *Physics of Dry Granular Material*, Vol. 350 of *NATO Advanced Study Institute*, edited by H. J. Hermann and J. P. Hovi (Kluwer Academic Publishers, Dordrecht, 1998), pp. 232,233.
[10] G. Mandl, L.N. de Jong, and A. Maltha, Rock Mech. **9**, 95 (1977).
[11] M. Oda, J. Konishi, and S. Nemat-Nasser, Mech. Mater. **1**, 269 (1982).
[12] E. Aharanov and D.W. Sparks, Phys. Rev. E **60**, 6890 (1999).
[13] R.L. Biegel, C.G. Sammis, and J.H. Dieterich, J. Struct. Geol. **11**, 827 (1989).
[14] C.G. Sammis and S.J. Steacy, Pure Appl. Geophs. **142**, 777 (1994).
[15] M. Cates, J. Wittmer, J. Bouchaud, and P. Claudin, Phys. Rev. Lett. **81**, 1841 (1998).
[16] S. Ouaguenouni and J.N. Roux, Europhys. Lett. **39**, 117 (1997).
[17] P.A. Cundall and O.D. Strack, Geotechnique **29**, 47 (1979).
[18] S. Nasuno, A. Kudrolli, and J. Gollub, Phys. Rev. Lett. **79**, 949 (1997).
[19] C.G. Sammis, R. Osborne, J. Anderson, M. Banerdt, and P. White, Pure Appl. Geophs. **124**, 53 (1986).
[20] S.B. Savage and M. Sayed, J. Fluid Mech. **142**, 391 (1984).
[21] N. Beeler and T. Tullis, J. Geophys. Res. B **102**, 22,595 (1997).
[22] F. Radjai, M. Jean, J. Moreau, and S. Roux, Phys. Rev. Lett. **77**, 274 (1996).
[23] C.H. Liu, S.R. Nigel, D. Schecter, S.N. Coppersmith, and S. Majumadur, Science **269**, 513 (1996).
[24] F. Radjai, D.E. Wolf, M. Jean, and J.J. Moreau, Phys. Rev. Lett. **80**, 61 (1998).
[25] L. Rothenburg and R.J. Bathurst, Geotechnique **39**, 601 (1989).
[26] J. K. Morgan and M. S. Boettche, J. Geophys. Res. **104**, 2703 (1999).
[27] J. K. Morgan, J. Geophys. Res. **104**, 2721 (1999).
[28] M. Oda and K. Iwashita, Int. J. Eng. Sci. **38**, 1713 (2000).
[29] D. Howell, R. Behringer, and C. Veje, Phys. Rev. Lett. **82**, 5241 (1999).
[30] P.K. Haff, J. Fluid Mech. **134**, 401 (1983).
[31] F. Lacombe, S. Zapperi, and H.J. Hermann, Eur. Phys. J. E **2**, 181 (2000).
[32] C. H. Scholz, *The Mechanics of Earthquakes and Faulting* (Cambridge University Press, New York, 1990).
[33] C. Marone and C.H. Scholz, J. Struct. Geol. **11**, 799 (1989).
[34] D. W. Sparks and E. Aharanov, in *Proceedings of the 2nd ACES Workshop*, edited by M. Matsuura, K. Nakajima, and P. Mora (APEC Cooperation for Earthquake Simulation, University of Queensland, Brisbane, Australia, 2001), pp. 77–82.
[35] C. Ancey and P. Evesque, Phys. Rev. E **62**, 8349 (2000).